Flow of Foams

Katgert, G.

Chapter 2

Linear shear of two dimensional foams

In this chapter, we first review recent research on the rheology of two dimensional foams. We then describe experiments to unravel the connection between local and global behaviour in a two-dimensional foam. To this end we have focused on average velocity profiles in ordered and disordered two-dimensional foams which are covered by a glass plate, and which are linearly sheared. We show that the shape of these profiles can be understood by a model that takes into account viscous dissipation at the bubble scale. We verify our claims by rheometrical measurements. Our results strongly suggest that disorder leads to anomalous scaling of the drag forces: for bidisperse two-dimensional foams, the functional form of the averaged dissipation between bubbles differs markedly from the dissipation between two bubbles moving with constant speed with respect to each other.

2.1 Overview of the field

Experimentally, the rheology of three-dimensional foams (and emulsions) has been studied extensively, mainly in oscillatory strain ([37] and references therein), but recently, the rheology of monolayers of foam bubbles has received increasing attention [8, 9, 12]. Three experimental configurations can be encountered in the literature: the *bubble raft*, see Fig. 2.1(a) where bubbles float freely at the surface of a soapy solution [31], a liquid-

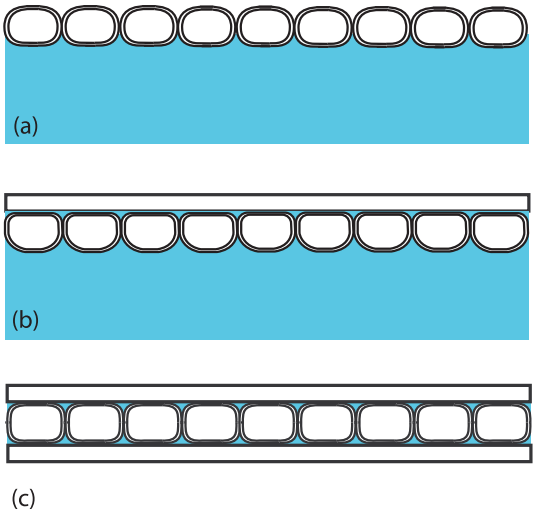

FIGURE 2.1: Various geometries used in (quasi) two-dimensional foam rheology experiments: (a) freely floating bubble raft, (b) bubble layer confined between liquid surface and glass plate, (c) Hele-Shaw cell: bubble layer confined between two glass plates.

glass setup where bubbles are sandwiched between a glass plate and the surface of the soapy solution [64,65], see Fig. 2.1(b) and the *Hele-Shaw cell*, see Fig. 2.1(c), where bubbles are squashed between two glass plates [9].

These configurations have a number of advantages over three-dimensional systems. First, drainage is absent since the systems extendo only in a horizontal plane. Second, in contrast to three-dimensional foams, which are opaque and which one can only probe with diffusive wave scattering [37] and X-ray tomography [53], the position of all bubbles can be tracked at all times. By doing so, one can investigate the connections between the behaviour of the individual bubbles and the global flow.

In what follows we will describe experiments on the rheology of two-dimensional foams, and therefore we will first discuss recent literature on the rheological behaviour of the above-mentioned systems.

The determination of the static, elastic properties of two dimensional foams, such as the scaling of the shear moduli with packing fraction, is largely an unexplored terrain, even though much theoretical effort has been devoted to precisely that part of foam physics [1]. Instead, experi-

mentally, various groups have looked at shear startup and steady flow of two dimensional foams [8, 9, 12, 66, 67]. The analysis of such experiments comprises for a large part of a host of different statistical measures such as the distribution of stress drops [8, 36, 71], statistical properties of bubble motions such as velocity fluctuations [9, 68] and the spatial distribution of T1 events [66, 69, 70]. While each experiment was analysed in a different way, in all experiments averaged velocity profiles have been measured. Due to the variation in experimental geometries that have been employed, connecting results remains difficult, as we will discuss in the next section.

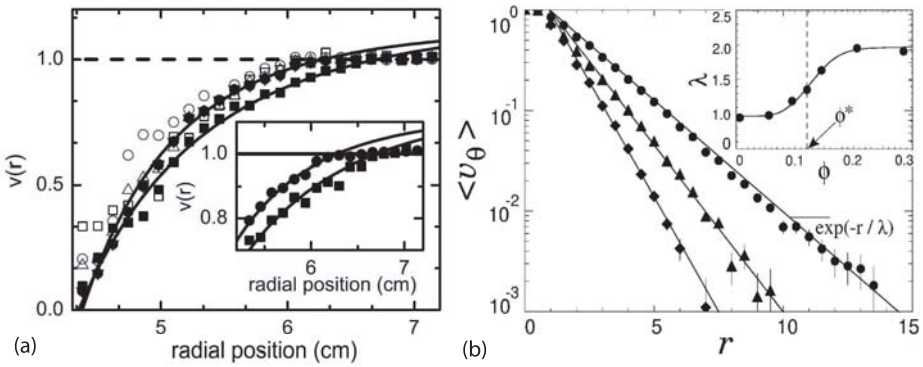

FIGURE 2.2: (a) Velocity profiles of bubble raft in Couette geometry (outer cylinder rotating) for 2 different rates of strain: $\Omega = 5 \times 10^{-3}$ (■) and $\Omega = 8 \times 10^{-4}$ (●). Inset zooms in on region of discontinuity. Open symbols are not relevant in our discussion (Figure reproduced from [68]). (b) Velocity profiles for bi-disperse foam between two glass plates (inner cylinder rotating): $\phi = 0.95$ (♦), $\phi = 0.85$ (▲), $\phi = 0.80$ (●). Profiles are fitted with $\exp(-r/\lambda)$, the inset shows variation of λ with $1 - \phi = \phi_l$ (Figure reproduced from [9].)

Velocity profiles

The flow of foams has been studied in a Taylor-Couette geometry, which consists of two concentric cylinders with the foam in between, in both the Hele-Shaw [9] and bubble raft [8, 68] configuration. Lauridsen, Twardos and Dennin [8, 68, 71] drove a polydisperse bubble raft by a rotating outer

cylinder at low strain rates and measured the averaged velocity profile of the foam and the stress on the inner cylinder as a function of strain rate. The averaged velocity profile exhibits a discontinuity in the strain rate, see Fig. 2.2(a): away from the outer (driving) wheel the azimuthal velocity is constant and equal to the angular velocity of the outer cylinder, until at some $\dot{\gamma}$-dependent critical radius r_c the velocity profile discontinuously starts decaying. The decaying part was well fitted by with a velocity profile expected for a Herschel-Bulkley fluid, for which we repeat the constitutive relation here

$$\tau = \tau_Y + \mu\dot{\gamma}^n, \tag{2.1}$$

The authors find $n = 0.45$ for $\Omega = 8 \times 10^{-4}$ and $n = 0.33$ for $\Omega = 5 \times 10^{-3}$ [68]. In this experiment, the packing fraction ϕ was fixed at 0.9.

Debrégeas, Tabuteau and Di Meglio sheared a bidisperse foam in a Hele-Shaw cell at low strain rates (within a velocity range in which the shape of the velocity profiles was found to be independent of the strain rate). Away from the driving cylinder, the azimuthal velocity was seen to decay exponentially. The authors also varied the liquid content in the cell, and hence ϕ, and observed the localisation length to grow for decreasing packing fraction, see Fig. 2.2(b).

Although both systems are similar in that the distribution of T1 events is proportional to the gradient $\frac{\partial v_\theta}{\partial r}$ [62, 68], the differences between the experiments, such as the discontinuous versus continuous velocity profiles, are more pronounced. This is surprising, since both experiments are performed at low rotation velocity and the experimental setups are very similar, apart from the upper and lower boundaries.

Recent developments

We try to understand the rheology of foams through measurements of averaged velocity profiles. Some recent papers have guided our thoughts on this subject. It has long been stated that, if one is measuring at sufficiently low strain rates and the associated timescale is slower than all kinematic relaxation times, the presence of confining boundaries, such as in the Hele-Shaw cell, should not matter. In this regime the experiments were said to be performed in the *quasistatic limit* [9, 66, 72, 73]. The rate independence of the velocity profiles at low strain rates was then invoked as proof that the system was in this limit. In a recent paper, however,

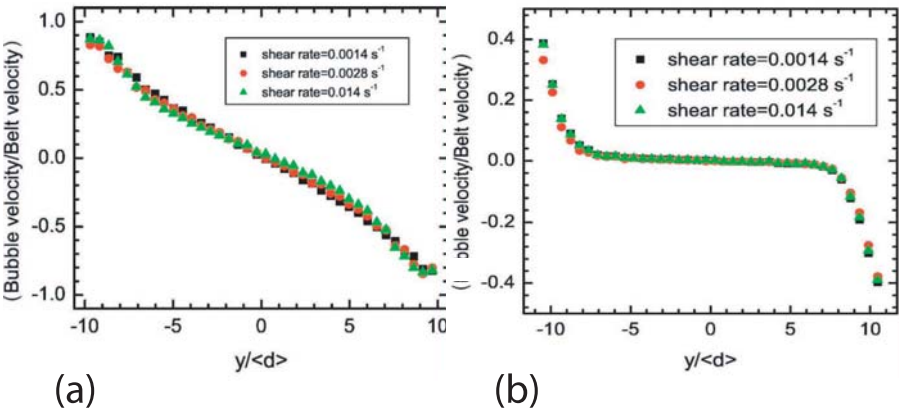

FIGURE 2.3: (a) Averaged velocity profiles for linearly sheared bubble raft, rescaled by driving velocity. (b) averaged velocity profiles for linearly sheared foam layer between glass plate and liquid, rescaled by driving velocity. Note the slip with respect to the driving bands. Figures reproduced from [66].

the influence of these boundaries on the shape of velocity profiles in shear flows of two-dimensional foams has been examined [66]. A mono-disperse foam at fixed ϕ_l was sheared linearly by two counter-propagating conveyor belts. The foam layer was either floating freely or confined between a glass plate and the liquid surface. For both geometries, the resulting velocity profile exhibits rate independence, but its shape is strongly dependent on the boundary: for the bubble raft, the averaged velocity profile is quasi-linear, see Fig. 2.3(a), resembling plane-Couette flow of Newtonian liquids, but the confined foam shows exponentially decaying shear bands, see Fig. 2.3(b). We have already seen that the flow of bubbles along a solid boundary (the top plate) leads to dissipation, and this apparently influences the dynamics of the bubbles.

An analytical model, taking into account this viscous friction with respect to a boundary, is proposed in [10]. The foam is described as a Bingham fluid experiencing a frictional body force which depends linearly on the velocity, allowing for analytical treatment of the problem. The result-

ing stress balance reads as follows:

$$\beta v = \frac{\partial}{\partial y}\left(\tau_Y \tanh(\gamma/\gamma_Y) + \eta\dot{\gamma}\right), \tag{2.2}$$

with a strain dependent yield stress τ_Y that saturates at the yield strain. For large strains (or steady shear) and relatively high strain rates the velocity profiles converge to exponential decay, but for vanishing friction coefficient (i.e in the case of a bubble raft) the decay length is of the order of the system size and the flow profile closely resembles a Newtonian flow profile. The exponentially decaying velocity profiles in the case of an additional wall drag can hence be understood as a result of the balance of the body force (the wall drag exerted on the foam bubbles) with enhanced gradients in the local velocities, resulting in gradients in the local strain rate.

2.2 Linear shear of two dimensional foams

We induce a linear shear flow in a two-dimensional foam. We record averaged velocity profiles and by fitting these profiles to solutions of a drag force balance model we can investigate the viscous stresses inside the foam. The scaling with strain rate of these viscous stresses can be compared to the scaling of the local bubble drag, as well as with the global flow curve, though rheometry.

2.2.1 Experimental details

We create a bidisperse monolayer of foam bubbles of 1.8 and 2.7 mm diameter on the surface of a reservoir of soapy solution, consisting of 80% by volume demineralized water, 15% glycerol and 5% Blue Dawn dishwashing agent (Proctor & Gamble), by bubbling nitrogen through the solution via syringe needles of variable aperture. We measure the bath surface tension σ with the pendant drop method [74] and find σ = 28 mN/m. We measure the dynamic viscosity η with a Cannon Ubbelohde viscometer and find η = 1.8 mPa.s.

Setup

The bubbles are contained inside an aluminum frame (400 x 230 mm) which can be leveled with the liquid surface and can support the glass boundary to which the bubbles bridge once it is in place. The glass boundary consists of 3 glass plates with slits to accommodate two PMMA wheels of radius 195 mm and thickness 9.5 mm. The gap between the liquid surface and the glass plates is fixed at 2.25 ± 0.01 mm, such that the packing fraction is fixed. We will show in chapter 4, that for this gap the packing fraction is $\phi = 0.965 \pm 0.005$. The wheels, which are grooved to provide a no-slip boundary for the bubbles, can be lowered into and raised out of the solution through the slits. The wheels are connected to two Lin Engineering stepper motors, each driven by microstepping driver, and are rotated in opposite directions. As a result, the layer of bubbles is sheared with a driving velocity $v_0 = \omega r_0$ in the plane of the bubbles, see Fig. 2.4(b). At any point along the line where the wheels contact the foam bubbles the horizontal component of the driving velocity is given by $v_0 = \omega r_1 \cos\phi$. But $r_1 = \frac{r_0}{\cos\phi}$ and hence $v_0 = \omega \frac{r_0}{\cos\phi} \cos\phi = \omega r_0$ and the foam is driven with this velocity all along the contact line of 230 mm, see Fig. 2.4(b).

No motion is observed due to the vertical component of the radial velocity, although bubbles do leave the system, while being pinned to the wheels, at the edges of the slits. However, no holes are produced in the two dimensional foam layer as a result of this, either because at high driving velocities the bubbles reenter the system before rupturing while traveling on the wheel, or because at low velocities bubbles from outside the shearing region are pushed inwards due to the bubble surplus at the edges. The resulting driving velocity gives rise to a global strain rate $\dot{\gamma} = 2v_0/W$, where W denotes the gap between the wheels, which can be varied between 5 and 10 cm.

Imaging and Analysis

The velocity profiles are obtained from images which we record by a Foculus BW 432 CCD camera equipped with a Tamron 28-300 telezoom objective. A typical image is shown in Fig. 2.5. To improve the brightness and obtain images in which the bubbles are represented by circles (see Fig. 2.4(c) for an example), the foam is lit laterally by two fluorescent tubes, each driven by high frequency ballasts to prevent flickering in the

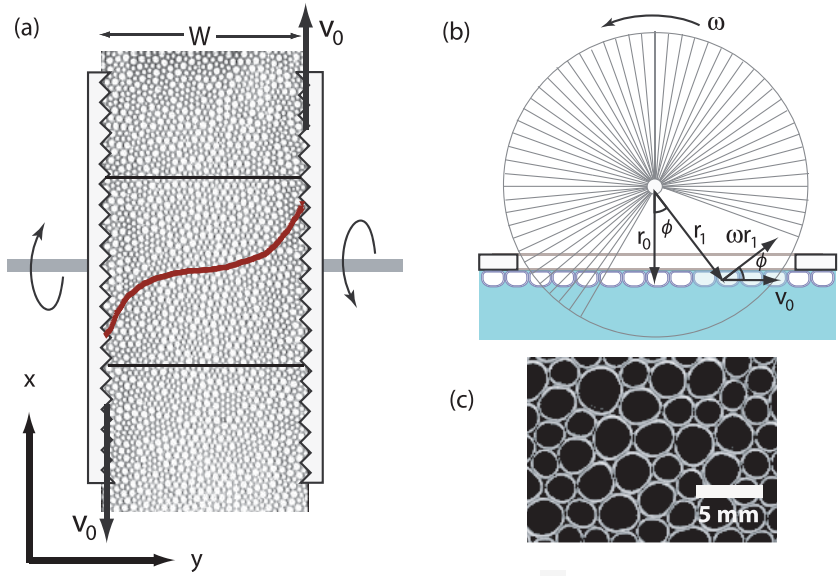

FIGURE 2.4: (a) Schematic topview of the experimental setup. W represents the gap width and the two horizontal lines indicate the edge of the region over which the velocity profiles are calculated. The red curve depicts one such profile.(b) sideview of shearing wheels. The slits in the glassplate are drawn for clarity. Explanation of the x independence of v_x at the liquid surface. (c) Experimental image of the foam, the scalebar represents 5 mm.

images. The bottom of the reservoir is covered with a black plate to improve contrast. The frame rate is fixed such that the displacement at the wheels is fixed at 0.15 mm between frames and we take 1000 frames per run, corresponding to a strain of 3.75 for a 4 cm gap. In the images, 1 pixel corresponds to approximately 0.1 mm.

We obtain the velocity profiles through particle tracking and a Particle Image Velocimetry-like technique: for each y-value, we calculate the cross-correlation $(X_n)^2$ between the corresponding image line $P_n(x)$ of length m and the same image line $P_{n+1}(x)$ in the next frame shifted by an amount τ:

$$X_n(\tau)^2 = \sum_{i=0}^{m-\tau} P_n(i)P_{n+1}(i+\tau). \tag{2.3}$$

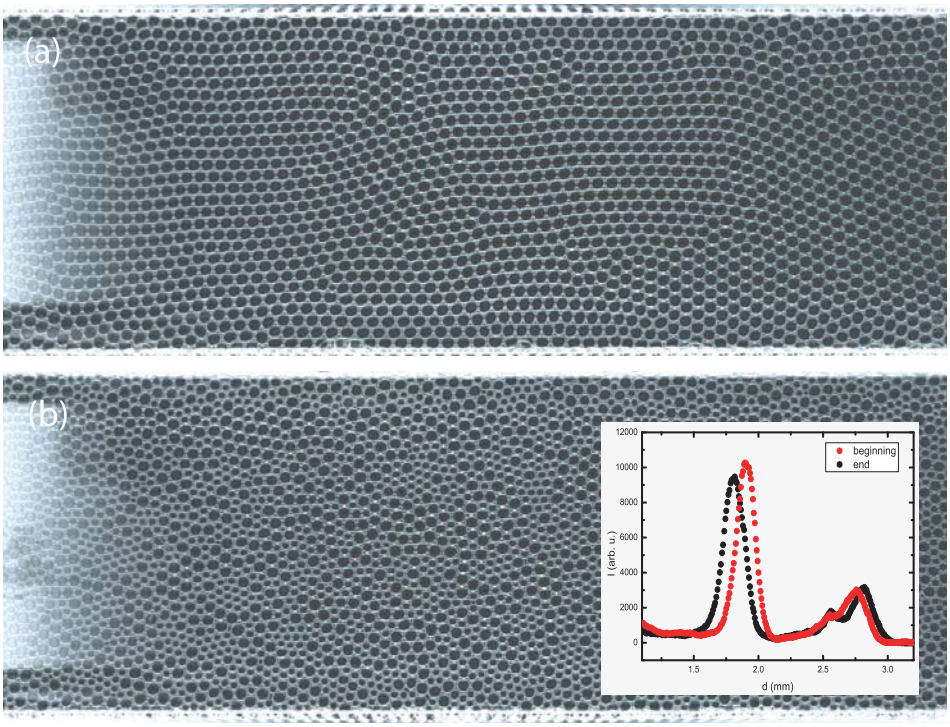

FIGURE 2.5: (a) Images of sheared regions for both (a) monodisperse and (b) bidisperse foams. Inset shows size distribution and coarsening over the duration of an experimental run for bidisperse foams.

We can then proceed in two ways. One option is to, for each y-value, add up all cross-correlations from all frames and calculate the average displacement $\Delta x(y)$ per frame by fitting a parabola to the resulting sum of cross-correlations and taking the peak value of that parabola:

$$\Delta x(y) = \max\left(\sum_{n=0}^{999}(X_n(\tau))^2\right). \tag{2.4}$$

Alternatively, we can fit a parabola to each cross-correlation separately and obtain the average displacement by averaging the maxima of all individual parabolas:

$$\Delta x(y) = \sum_{n=0}^{999}\max\left((X_n(\tau))^2\right). \tag{2.5}$$

By comparing to average velocity profiles obtained by particle tracking [75], we find that the latter procedure gives the closest match to the tracking velocity profiles, and we have employed that procedure throughout. We restrict ourself to the central 60 mm of the shearing region, see Fig. 2.4(a), to avoid effects caused by the recirculation of the foam at the edges of the wheels. We thus obtain both spatially (in the x-direction) and temporally averaged velocity profiles. Note that for disordered foams the flow is strongly intermittent, with large fluctuations in bubble velocities and positions. Nevertheless, we obtain smooth reproducible velocity profiles with the above method.

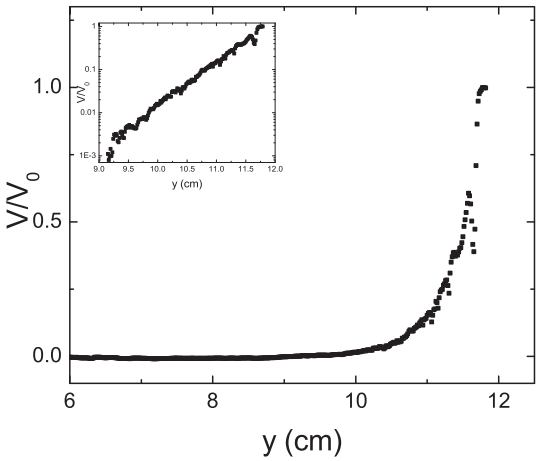

FIGURE 2.6: Flow at the liquid surface in the absence of bubbles, as imaged by depositing silver powder. Inset: same profile on lin-log scale, showing exponential decay away from the boundaries.

We check that the drag on the foam bubbles due to flow of the bulk liquid underneath is negligible by measuring the velocity profile of bubbles floating on a very shallow layer of bulk fluid. In this case the fluid surface velocity is decreased due to the no-slip boundary condition at the reservoirs bottom. This does not alter the profiles. We furthermore measure the velocity profile of the liquid surface itself at the same fluid level as in the foam experiments ($\approx$ 3.5 cm) by imaging the flow of silver particles that were sprinkled on the liquid surface, see Fig. 2.6. We observe an exponentially decreasing velocity profile at the fluid surface, which implies

that even if the fluid drag were of the order of the other drags acting on the bubbles, it would not significantly alter the flow profiles except near the wheels.

To check whether coarsening occurs we measure the bubble size distribution by measuring the surface area of the rings in the images. We obtain sharply peaked size distributions, see inset in Fig. 2.5(b), that show about 3 % coarsening over the duration of the runs, which corresponds to about 2 hours.

2.2.2 Results

Disordered foams

We now focus on averaged velocity profiles in disordered two-dimensional foams. These foams are produced by bubbling a fixed flow rate of nitrogen through syringe needles of 2 different inner diameters, such that bubbles of 1.8 $\pm$0.1 and 2.7 $\pm$0.2 mm result. The bubbles are gently mixed with a spoon until a disordered monolayer results. For gap widths of 5, 7 and 9 cm, we drive the foam at 6 different velocities, spanning 2.5 decades: $v_0 =$ 0.026, 0.083, 0.26, 0.83, 2.6 and 8.3 mm/s.

Note that we perform the sweep in driving velocities from fast to slow and that we preshear the system for one full wheel rotation, to start with bubbles covering the wheel. This is done to ensure the packing fraction remains constant during the strain rate sweep; when the entire circumference of the wheel is covered with bubbles a balance results between bubbles dragged out of the system and injected back in. If we would sweep from slow to fast driving rates, this balance is not achieved, resulting in a packing fraction that decreases during the experiment. To fix the packing fraction, we fix the gap between glass plate and liquid surface at 2.25 $\pm$ 0.01 mm.

Results are plotted in Fig. 2.7: the profiles exhibit shearbanding, and for all gap widths the profiles become increasingly shear banded at increasing driving velocities. The slowest runs at W = 5 cm yield essentially linear velocity profiles. We suggest that this is due to the small gap width, which results in overlapping shear banded profiles resembling a linear profile, and we will present a model in section 2.2.3 that supports this conclusion.. This is further illustrated in Fig. 2.7(d): there we plot the velocity profile for a driving velocity of 0.26 mm/s for all three gap widths

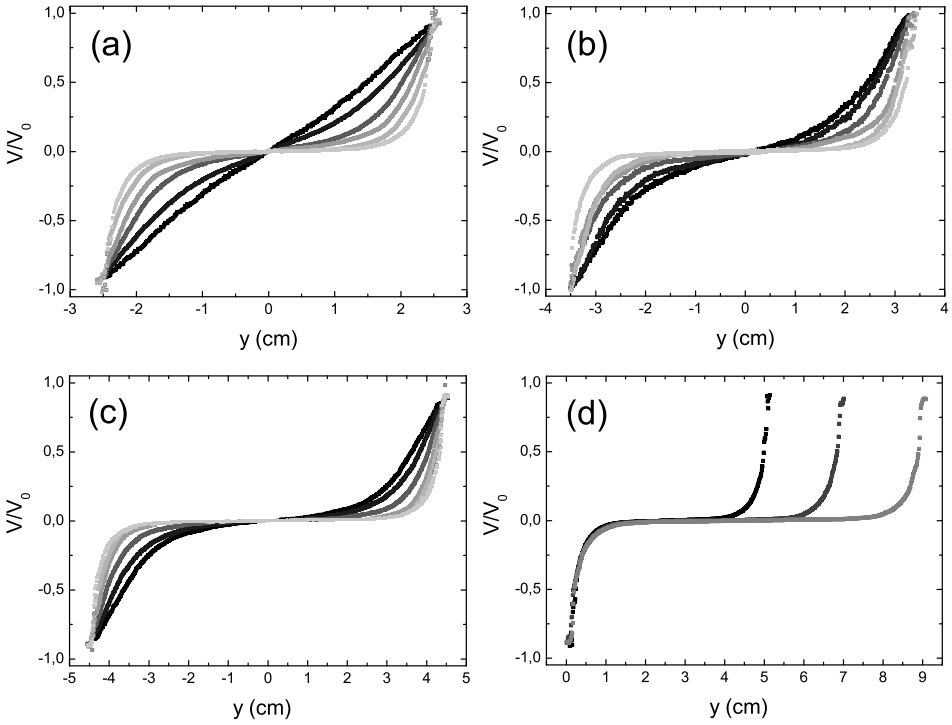

FIGURE 2.7: Profiles for a gap width $W = 5$ (a) 7 (b) and 9(c) cm. From black to light grey, $v_0 = 0.026$ mm/s, 0.083 mm/s, 0.26 mm/s, 0.83 mm/s, 2.6 mm/s and 8.3 mm/s. For all gap widths we observe that the localisation near the driving wheels increases for increasing driving velocity. (d) Profiles at 2.6 mm/s for all three gap widths. Regardless of the gap width all profiles decay at the same rate.

together, which clearly shows that for all widths, the velocity profiles decay at the same rate. Fig. 2.7(d) thus hints that in this experiment the driving velocity at the edges, instead of the overall shear, sets the velocity profiles. Therefore the local response to forcing will provide the key towards understanding the shape of these profiles. Note finally that the profiles do not exhibit slip with respect to shearing wheels, except for the fastest runs.

2.2.3 Model

We now propose a model to account for the shear banding behaviour discussed above. We ignore the elastic energies in the system and only consider the viscous drags. The relevant drag forces in our system have already been discussed in section 1.2.4 and we will do so once more: F_{bw}, the drag force per bubble sliding past a solid wall, scales as

$$F_{bw} = f_{bw}(Ca)^{2/3} = f_{bw}\left(\eta v/\sigma\right)^{2/3}, \tag{2.6}$$

with η the bulk viscosity, σ the surface tension and f_{bw} a constant with dimensions of force. Typically $f_{bw} \propto \sigma r_c$ [18], with r_c the radius of the deformed contact between bubble and wall. We remind the reader that for bubbles in a soapy solution, the 2/3 scaling with Ca only holds for surfactants that are mobile [20], see section 1.2.4. Results from [4] strongly indicate that this is indeed the case for Dawn, and we will later confirm that this scaling applies to our system.

The drag force between 2 bubbles sliding past each other has not received much attention up to now, although [24] provides indirect evidence that it scales like F_{bw}, i.e. $F_{bb} \propto (\eta \Delta Ca)^{\zeta}$, with $\Delta Ca \equiv \eta \Delta v/\sigma$. In a very recent paper it is explicitly shown that it scales indeed as $(\Delta Ca)^{\zeta}$, [25]. The authors find $\zeta = 0.5$, although various physico-chemical peculiarities, as well as the range of Ca one measures in, can alter this exponent. Note that the physical mechanism leading to this scaling is markedly different from that leading to the nontrivial scaling of the bubble-wall drag: the viscous drag between a bubble and a wall is due to the variations in thickness of the thin film separating the two, whereas in this case it is actually the size of the deformed facet that changes when two bubbles come into contact and slide past each other.

Taking all of this into consideration, it seems reasonable to assume

that:

$$F_{bb} = f_{bb}\,(\eta \Delta v/\sigma)^{\zeta}\,, \tag{2.7}$$

again with $f_{bb} \propto \sigma\kappa_c$, with κ_c the radius of the deformed contact between bubbles.

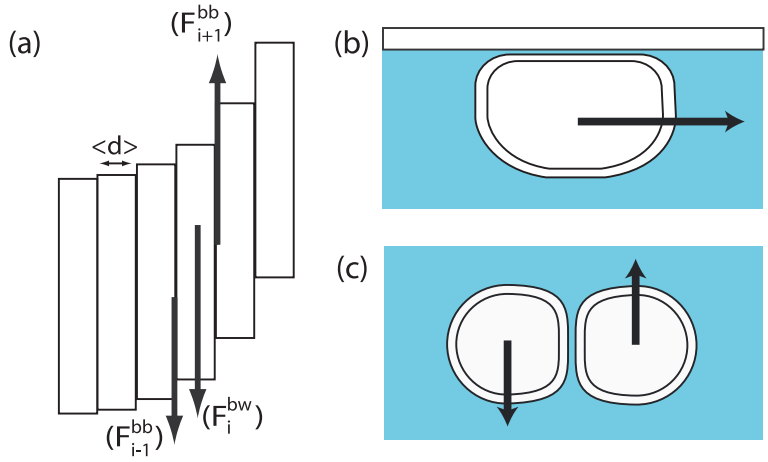

FIGURE 2.8: Illustration of drag balance model. The shear region is divided in lanes labeled i which all experience a drag force de to the top plate and due to both neighboring lanes. Illustration of the films around which the viscous drag forces act.

We now assume that at every y-position in the shearing region the average drag forces per bubble $\overline{F}_{bw}$ and $\overline{F}_{bb}$ scale in a similar way with velocity as the individual drag forces. In particular, we will assume that $\overline{F}_{bw} = f_{bw}(Ca)^{2/3}$, but that $\overline{F}_{bb} = f_Y + f_{bb}(\Delta Ca)^{\beta}$. We thus leave the possibility open that the averaged bubble-bubble drag forces scale differently from the drag froces experienced by single sliding pairs of bubbles. We divide our shearing region in lanes labeled i and assume that on every lane the time-averaged top plate drag per bubble $\overline{F}^{i}_{bw}$ balances with the time-averaged viscous drag per bubble due to the lane to the left ($\overline{F}^{i}_{bb}$) and right ($\overline{F}^{i+1}_{bb}$), see Fig. 2.8:

$$\overline{F}^{i+1}_{bb} - \overline{F}^{i}_{bw} - \overline{F}^{i}_{bb} = 0. \tag{2.8}$$

We assume that the averaged drag forces scale similar to the bubble drag force, but allow for a yield drag term in the interbubble drag, to remain consistent with rheometrical data presented later on and to reflect the elastic barrier bubbles have to overcome before they slide past each other, and write:

$$\overline{F}^{i}_{bw} = f_{bw}(\eta v_i/\sigma)^{2/3}\,, \tag{2.9}$$

$$\overline{F}^{i}_{bb} = f_Y + f_{bb}\left[(\eta/\sigma)(v_i - v_{i-1})\right]^{\beta}\,, \tag{2.10}$$

$$\overline{F}^{i+1}_{bb} = f_Y + f_{bb}\left[(\eta/\sigma)(v_{i+1} - v_i)\right]^{\beta}\,. \tag{2.11}$$

Note that assuming similar behaviour between the averaged drag forces and the local drag forces is a rather strong statement, given that, due to the intermittent and disordered bubble motion, the instantaneous bubble velocities are fluctuating and not necessarily pointing in the x-direction.

Inserting the expressions from Eq. (2.11) into Eq. (2.8) and defining $k = f_{bw}/f_{bb}$ we arrive at:

$$k\left(\frac{\eta v_i}{\sigma}\right)^{2/3} = \left(\frac{\eta}{\sigma}\right)^{\beta}\left[(v_{i+1} - v_i)^{\beta} - (v_i - v_{i-1})^{\beta}\right]\,. \tag{2.12}$$

Note that the yield drag contributions cancel, which is a particular advantage of the linear geometry we work in.

To actually solve Eq. (2.12) numerically, it turns out we need to take into account the discrete nature of both the bubbles and the pixels in the images, as the distance in Eq. (2.12) between the v_i's is not arbitrary, but set by the average bubble diameter $\langle d\rangle$. The forward difference on the bubble scale is

$$v_{i+1} - v_i = \langle d\rangle \cdot \frac{\partial v}{\partial y}|_{y=y_i}, \tag{2.13}$$

in differential form. In the images, however, the velocities are separated by the pixel size p. One can of course reverse Eq. (2.13) and write

$$\frac{\partial v}{\partial y}|_{y=y_i} = \frac{1}{p}(v_{i'+1} - v_{i'}) \tag{2.14}$$

to end up with the forward difference on the pixel scale. Combining Eqs. (2.13) and (2.14) and recognising that the full forward difference of Eq. (2.12) is given by

$$(v_{i+1} - v_i)^{\beta} - (v_i - v_{i-1})^{\beta} = \langle d\rangle^{1+\beta} \cdot \frac{\partial}{\partial y}\left(\frac{\partial v}{\partial y}\right)^{\beta}|_{y=y_i}, \tag{2.15}$$

we can write Eq. (2.12) in a form that is suited for numerical integration:

$$\frac{k}{(\langle d\rangle/p)^{1+\beta}} \cdot \left(\frac{\eta v_i}{\sigma}\right)^{2/3} = \left(\frac{\eta}{\sigma}\right)^{\beta} \left[(v_{i+1} - v_i)^{\beta} - (v_i - v_{i-1})^{\beta}\right] . \qquad (2.16)$$

2.2.4 Fits

Procedure

We compare all 18 runs to solutions of the model. We focus on the central part of the data where $|v| < 3/4 v_0$ to avoid the considerable edge effects near the shearing wheels (for instance the bumps in the low-velocity profiles in Fig. 2.7(a) and the slip with respect to the wheel in the fast runs). Since the shape of the velocity profiles is set by the local velocity, we assume this is a valid procedure, and will not affect the shape of the model solution. We numerically integrate Eq. (2.16) from $y = 0$, where $v = 0$, to the y value for which $v = 3/4 \cdot v_0$, while keeping β and k fixed. The drag force balance should govern the shape of the velocity profiles for all driving rates and gap widths and hence, at fixed β, for all profiles we determine the k value that gives the best fit to the data. The k values exhibit a systematic variation that depends on the value of β one chooses, see Fig. 2.9(f), and by repeating the procedure for a range of β we determine the value for which the variation in k is minimized. We subsequently fix k and β and take these values to hold for all data sets.

Results

We capture the shape of all data sets with high accuracy by fixing k and β, whose values are $k = 3.75$ and $\beta = 0.36 \pm 0.05$ as extracted from Fig. 2.9(f). The results are plotted in Fig. 2.9, and we see that for these values all velocity profiles are adequately fitted except for the slowest runs at $W = 5$ cm. We attribute this to the observation that edge effects extend further into the shearing region for small gaps. Note that the model profiles exhibit linear tails, see Fig. 2.9(e), and that the experimental velocity profiles in the same figure exhibit approximately the same behaviour. We can thus conclude that both the experimental and model profiles do not decay exponentially, in contrast with results found in previous studies [9, 66].

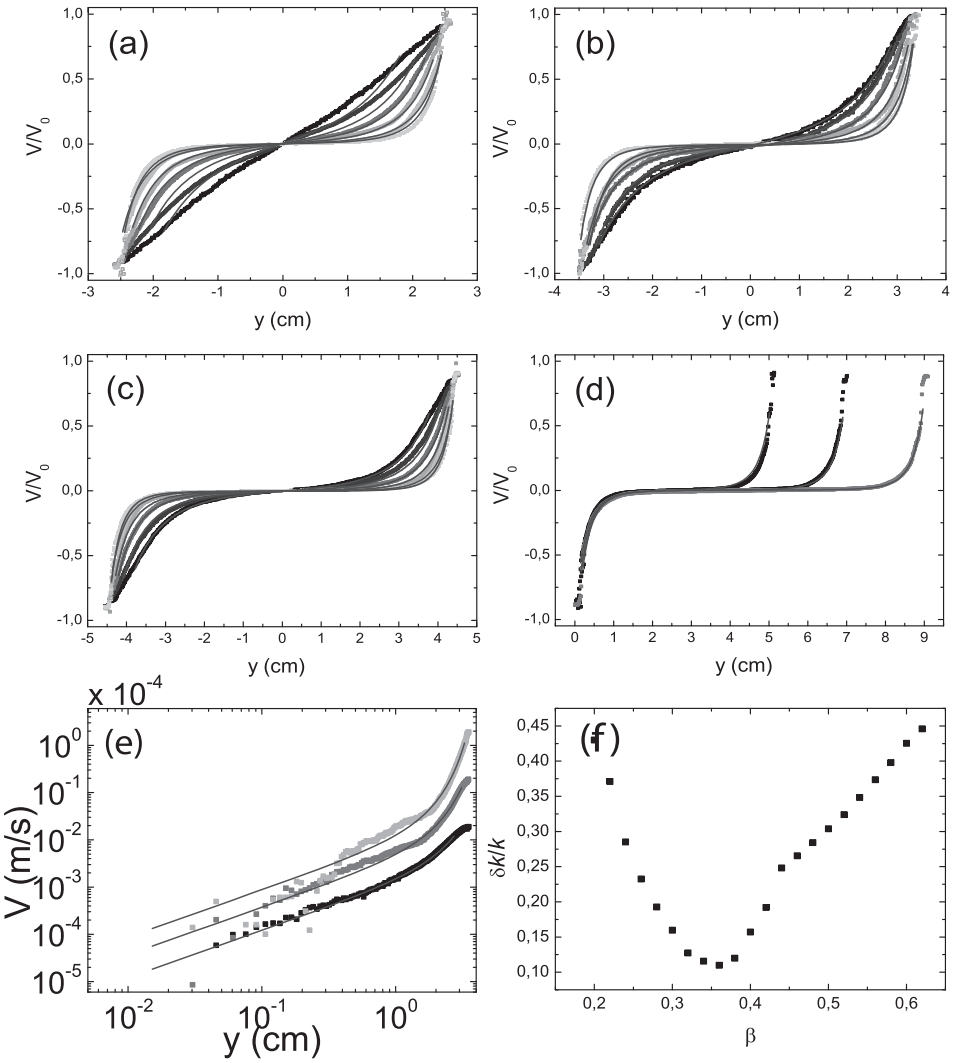

FIGURE 2.9: (a)-(d) Velocity profiles from Fig. 2.7 with model profiles obtained for $k = 3.75$ and $\beta = 0.36 \pm 0.05$. The model profiles fit the experimental data very well, except for the slowest runs at $W = 5$ cm gap. (e) Unrescaled velocity profiles for V_0 = 0.026 (black), 0.26 (grey) and 0.26 (light gray) mm/s and corresponding fits plotted on a log-log scale, to highlight the linear tails, in particular in the fit profiles. (f) Variance in k over all 18 runs for the bi-disperse foam as a function of β. A clear minimum at $\beta = 0.36$ can be observed.

2.2.5 Continuum Limit

We can take the continuum limit of Eq. (2.13) which reads:

$$f_{bw}\left(\frac{\eta v}{\sigma}\right)^{2/3}\langle d\rangle^{-1}=\frac{\partial\tau}{\partial y}\,, \tag{2.17}$$

The top plate drag can be considered as a body force and the interbubble drag force as the divergence of a shear stress τ:

$$\tau=\tau_Y+f_{bb}\left(\frac{\eta\langle d\rangle\dot{\gamma}}{\sigma}\right)^{\beta},\beta=0.36, \tag{2.18}$$

where τ_Y is an undetermined yield stress. This is the constitutive equation for a Herschel-Bulkley fluid [45] encountered before. We can now associate the averaged bubble drag force scaling at the local level with the power law scaling of the viscous stress in the Herschel-Bulkley model. The fact that the yield stress does not play a role for our velocity profiles can now be understood in two ways: firstly, since it is a constant it vanishes after taking the divergence of the shear stress, secondly, even though we include a yield stress term at the bubble scale, the contributions from both neighbouring lanes cancel in Eq. (2.12). Note that $\beta=0.36$ is remarkably close to the power law index $n=0.40$ found for the bulk rheology of three-dimensional mobile foams [20, 47] already discussed in Sec. 2.3 and to the values $n=0.33$ and $n=0.45$ found in [71] which were discussed in section 2.1.

2.3 Rheometrical determination of viscous forces in two-dimensional foams

To validate the assumptions made for the bubble-wall drag and the result obtained for the scaling of the local viscous friction inside the foam, in this section we will investigate the viscous forces that act at the bubble scale by rheometry. We use an Anton Paar DSR 301 rheometer, which can be operated in stress controlled mode and, through a feedback loop, also in strain controlled mode. We use the rheometer in strain controlled mode to investigate $\overline{F}_{bw}$. Moreover, we compare measurements, which we argue to reflect the actual drag force at the single bubble level F_{bb},

with measurements of the averaged viscous drag force on a bubble in a disordered flow of foam $\overline{F}_{bb}$.

2.3.1 Bubble-wall drag

We directly measure the bubble-wall friction with a method that was introduced in [20]. We load a monolayer of bubbles (d = 2.4 $\pm$ 0.1 mm) between two PMMA plates of radius R_P = 2 cm. The bubbles are pinned to the lower plate by means of a hexagonal pattern of indentations of size $\mathcal{O}(d)$, and can slip with respect to the smooth upper plate which is connected to the rheometer head. We measure the torque exerted by the bubbles as a function of the angular velocity of the smooth plate.

FIGURE 2.10: Close-up photograph of the rheometrical tool used to measure the bubble-wall drag. The radius r_c is clearly visible in reflected light and is used to extract R_0.

We convert $T(\omega)$ to $\overline{F}_{bw}(Ca)$ in the following way: each bubble exerts a wall stress $\tau_w = \overline{F}_{bw}/\pi R_0^2$ on the smooth plate. We integrate the contribution to the torque of this wall stress over the plate:

$$T = \int_0^{R_P} \tau_w r 2\pi r dr = \int_0^{R_P} \frac{\overline{F}_{bw}}{R_0^2} 2r^2 dr. \tag{2.19}$$

If we now assume that $\overline{F}_{bw} \propto [Ca]^\alpha = \left[\frac{\eta\omega r}{\sigma}\right]^\alpha$, we can immediately read of

from the data that $\alpha = 0.67$, see Fig. 2.11(a), so inserting this expression in the integral Eq. (2.19) yields:

$$T = \frac{2\overline{F}_{bw} R_p^{3.67}}{3.67 R_0^2}. \tag{2.20}$$

Since the bubbles are flattened during the measurement, we can only measure r_c by looking at the reflection of the deformed facet, see Fig. 2.10. We find $r_c = 1.59$ mm. As the bubble radius is smaller than κ^{-1} we can express R_0 in terms of r_c through $R_0^2 = \sqrt{\frac{3}{2}} r_c \kappa^{-1}$ (see chapter 1, section 2.3). Note that this derivation of r_c in terms of R_0 hinges on the assumption that the bubbles are not too deformed, which is not obvious in the rheometrical geometry, but for lack of a more precise relation we use it. We finally rescale the horizontal axis by multiplying ω with $\eta R_p/\sigma$. The resulting curve is plotted in Fig. 2.11(a).

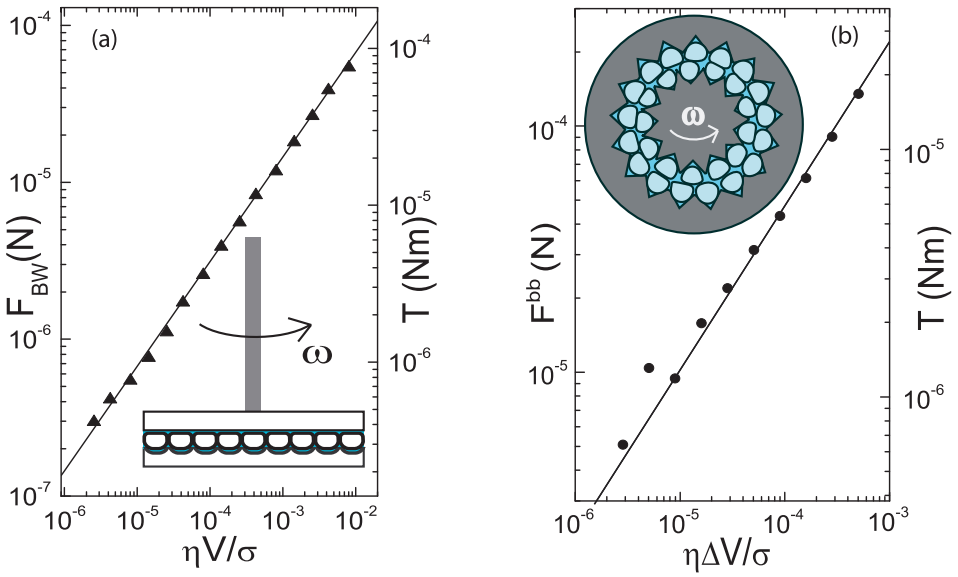

FIGURE 2.11: (a) Drag force per bubble exerted on smooth rotated plate as a function of Ca. The solid line represents $0.0015 \pm 0.0001 \cdot (\eta v/\sigma)^{2/3}$. The inset shows experimental geometry. (b) Drag force per bubble exerted by neighbouring, ordered lane of bubbles in a geometry that mimics the ordered sliding of bubble lanes. The solid line represents $0.022 \pm 0.002 \cdot (\eta \Delta v/\sigma)^{2/3}$.

2.3.2 Bubble-bubble drag

Drag at the bubble scale

To measure the power law scaling of the inter-bubble drag we abandon the linear geometry for a moment and actually measure the torque exerted by a foam driven at a strain rate $\dot{\gamma}$ in a cylindrical Couette geometry, which consists of an inner driving wheel, connected to the rheometer head, rotating inside an outer ring. This is a natural geometry to perform rheometry in. We will get back to the peculiarities of foam flow in a cylindrical geometry in chapter 3. The rheometrical experiments are performed with bubble rafts, i.e. foams that are not confined by a top plate, as the additional stresses due to the wall would disturb a clean rheological measurement.

Both boundaries are grooved to ensure a no slip boundary for the bubbles, of which a monolayer floats in the shearing region. We start with measuring $\overline{F}_{bb}$ for the ordered case by keeping the gap between the cylinders such that exactly two layers of bubbles fit in, see the inset of Fig. 2.11(b). The inner radius (r_i) is 1.25 cm and the outer radius (r_o) is 2.5 cm. We deposit 6mm diameter bubbles in the grooves, make sure that all bubbles are strictly pinned and remain in their groove, and vary the rotation rate ω of the inner cylinder over 2.5 decades while measuring the torque averaged over one rotation. The result is plotted in Fig. 2.11(b): even though the torque fluctuates enormously due to the elastic barrier the bubbles have to overcome before they can pass a neighbour, the force per bubble averaged over many such events scales with the dimensionless velocity difference as a power law with index 2/3, just as the wall drag scales with bubble velocity. No signs of a yield stress are observed, and we believe this is due to the fact that all elastic energy that is stored in the bubble deformation is released after yielding, such that one measures purely the viscous drag.

We multiply ω by $\eta r_i/\sigma$ to rescale to the dimensionless velocity difference and we divide the torque by r_i and the number of bubbles pinned at the inner wheel (i.e 10) to obtain the averaged bubble-bubble drag force per bubble in the ordered case, and in these rescaled coordinates we have plotted the results in Fig. 2.11(b).

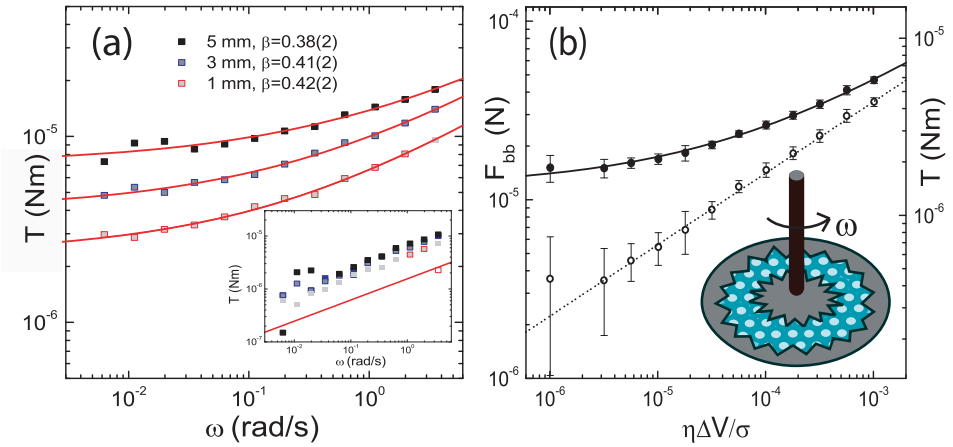

FIGURE 2.12: (a) Torque exerted on the inner wheel by a *monodisperse* foam in a Taylor-Couette geometry where the gap is of the order of 6-7 $\langle d \rangle$, for different bubble sizes. Fits are to Herschel-Bulkley model, power law indices β from fits are shown in graph. Inset shows same data with yield torque from fit subtracted, solid line is power law with index 0.4. Surprisingly, the yield stress increases with increasing bubble size. (b) Averaged drag force per bubble in a *bidisperse*, disordered foam. The foam is sheared in a Couette cell of inner radius 1.25 cm, outer radius 2.5 cm (hence a gap of 5 bubble diameters) without a top plate, see inset. We obtain $\overline{F}_{bb} = f_Y + f_{bb}(\Delta Ca)^\beta$, with the yield threshold $f_Y \approx 1.2 \pm 0.5 \times 10^{-5}$ N, $f_{bb} \approx 5.6 \pm 0.9 \times 10^{-4}$ N and $\beta = 0.40 \pm 0.02$ (solid line). Open circles are the same data with the yield torque obtained from the fit subtracted, which are well fit by a pure power-law with exponent 0.4 (dashed line).

From local to bulk viscous drag

We observe that the scaling exponent for the viscous drag at the bubble scale differs markedly from the scaling of the local viscosity inside the bulk foam as extracted from the velocity profiles, e.g., $\zeta = 2/3$ vs. $\beta = 0.36$. We hypothesize this is due to the disordered flow in the foam and will provide supporting evidence in what follows.

Still loading the cell with monodisperse foams with bubble radii of 1, 3 and 5 mm, we increase r_o to 8 cm, such that more layers of bubbles can fit inside the cell. However, since r_i is small, the curvature is high, which forces the foam to deviate from hexagonal packing during rotations. In this way we induce disorder through geometry. The resulting measurements, see Fig. 2.12(b), show clear yield stress behaviour and can be ex-

cellently fit by the Herschel-Bulkley model, yielding for all bubble sizes $\beta \approx 0.4$, which is markedly lower than the 2/3 found for the drag force in ordered lanes above, and close to the 0.36 extracted from the velocity profiles. Surprisingly, the yield stress appears to increase with increasing bubble radius, contrary to the intuition that the yield stress is set by the Laplace pressure and should hence scale in inverse proportion to the bubble radius. We attribute this to the deformation of the bubbles through the capillary flotation force, which is larger for larger bubbles and hence leads to a relatively larger contact size between the bubbles.

In order to convincingly establish a connection between the rheometrical data and the model, we now return to the geometry used for the ordered foams ($r_i = 1.25$ cm and $r_o = 2.5$ cm), and measure the torque exerted on the inner wheel by a *bidisperse* foam with the same bubble sizes as in the linear shear experiment. We obtain a clear confirmation that indeed the disorder changes the power law scaling of $\overline{F}_{bb}$: we again reproducibly measure Herschel-Bulkley behaviour with power law index $\beta \approx 0.40$, as can be seen in Figs. 2.12(b). To convert torques to $\overline{F}^{bb}$, we again divide by the number of bubbles and r_i. Since our outer rough boundary forces the bubble velocity to zero, we can rescale the angular frequency to the dimensionless velocity difference $\eta\Delta v/\sigma$ by assuming a linear velocity profile across the gap, decaying from ωr_i to 0. The gap width is approximately $6\langle d\rangle$ and hence we can estimate Δv. We extract from the rheological measurements an estimate for the ratio $k = f_{bw}/f_{bb} \approx 2.5 \pm 0.5$. This is close to the value $k = 3.75 \pm 0.5$ estimated from the flow profiles.

2.4 Discussion

The drag forces exerted on the bubbles by the top plate, which at first sight might be seen as obscuring the bulk rheology of the foam, enable us to back out the effective inter-bubble drag forces and constitutive relation of foams from the average velocity profiles. To further appreciate this fact, note that our model yields linear velocity profiles regardless of the exponent β if the body force due to the wall drag is zero.

By comparing the results obtained from the velocity profiles with the rheometrical measurements, we note a remarkable difference between the scaling of the bubble-bubble drag forces at the bubble level, which we have mimicked by strictly ordered bubble rheology, and the scaling at

the bulk level, which we have extracted from the velocity profiles and confirmed by rheometry: we find $F_{bb} \sim (\Delta v)^{2/3}$ at the bubble level and $\overline{F}_{bb} \sim (\Delta v)^{0.36}$ at the bulk level.

One might understand this anomalous scaling as follows: The degree of disorder does not affect the drag forces at the bubble scale, but it does modify the bubble motion. For disordered foams, the bubbles exhibit non-affine and irregular motion — hence they "rub" their neighbouring bubbles much more than when their flow is orderly, and consequently the averaged viscous dissipation is enhanced over what could naively be expected from the local drag forces [76]. This picture is corroborated by recent simulations on the bubble model [23], where one recovers this "renormalisation" of the drag force exponent [77, 78] and rate-dependent flow profiles [78].

In this vein, one could wonder why the drag with the top plate is not changed by the disordered motion of the foam bubbles. We have no definite answer, but we have verified, using tracking of the bubble motion, that the average of the instantenous bubble-plate drag force is very similar to the drag force calculated from applying the Bretherton result to the average velocity:

$$< (\vec{v}/|v|)_x |v|^{2/3} > \approx 0.9 < v_x >^{2/3} \quad . \tag{2.21}$$

On the other hand, the bubble-bubble drag force involves velocity *differences*, which therefore are much more broadly distributed, in particular when $\Delta v < v$ — apparently this causes the breakdown of the affine assumption.

Finally, the origin of the edge effects that prevent us from fitting our full experimental curves with the model profiles, might be due to the fluid drag near the wheels, as discussed in section 2.2.1. Alternatively the origin might lie in the absence of a local flow rule near the driving wheels as reported in [79]. One way to resolve this is accommodating non-local behaviour in our model, for instance by incorporating drag terms due to next nearest lanes, similar to the cooperativity length introduced in [79]. Nevertheless, since our model *is* local in spirit, it has enabled us to back out valuable information even though we have not been able to use the full velocity profiles.

2.5 Ordered foams

A final indication that indeed the disordered flow of the bidisperse foam is at the root of the anomalous scaling of the bulk viscosity with shear rate can be given by shearing ordered, monodisperse foams in the linear geometry, as was done in [66]. In this case the bubbles are expected to move affinely with the global shear, in which case one would expect the global viscous drag forces to scale the same as the local one.

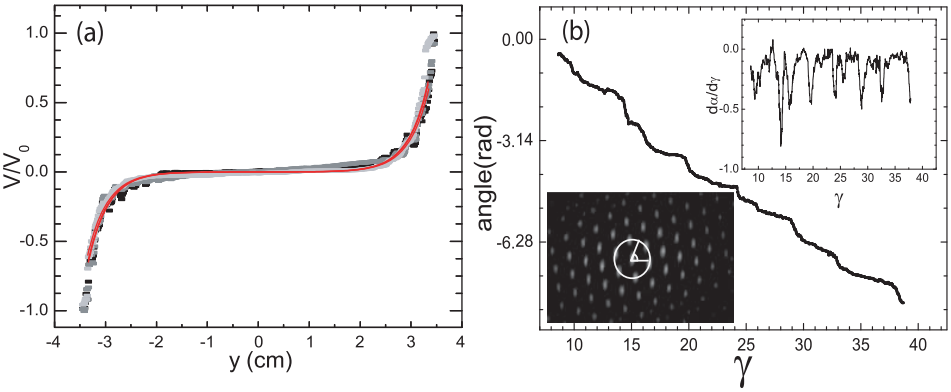

FIGURE 2.13: (a) Velocity profiles for a monodisperse, ordered foam with crystal axis aligned with the wheels. Gap $W = 7$ cm and $v_0 = 0.083$ (black), 0.26 (dark grey) and 0.83 (light grey) mm/s. Solid curves indicate fits to the model with $k = 0.3$, $\alpha = \beta = 2/3$. (b) Angle of the monodisperse foam with respect to the shearing direction as a function of strain (time): the foam remains stationary for considerable strains, after which it rapidly rotates over $\pi/3$. Upper inset shows derivative of main graph to highlight the apparent periodicity of the rotations. Lower inset shows 2D autocorrelation of foam image with the circle located at the first order maxima used to determine the rotation.

We shear a monodisperse, ordered foam with bubbles of size 2.7 mm, produced by blowing nitrogen through one syringe needle at fixed flow rate, at a gap W of 7 cm at $v_0 = 0.083, 0.26$ and 0.83 mm/s. We recover the rate independent and strongly shear banded velocity profiles reported in [66] (see Fig. 2.13). However, it turns out that the orientation of the hexagonal bubble packing with respect to the shearing direction of the foam is crucial for reproducibility: the monodisperse foam orients itself with one of its crystal axes parallel to the shearing boundaries and remains in that state for a considerable time, until it rather rapidly and

collectively rotates over an angle of $\pi/3$ radians until the next crystal axis is aligned with the wheels. We investigate this by taking the 2D-autocorrelation of the foam images taken from a run at 10 cm and measuring the pixel intensity along a circle located at the first order maxima, see inset of Fig. 2.13(b).

By cross correlating the intensity profile of the first image with that of later images, we obtain Fig. 2.13(b): the foam remains stationary for considerable strains, after which it quite rapidly rotates over $\pi/3$ radians and remains stationary again. The upper inset of Fig. 2.13(b) displays the derivative of the angle with time and confirms that stationary periods are interspersed with bursts, during which the foam rapidly rotates, and to which one could maybe even contribute a periodicity.

This remarkable phenomenon is, however, avoided by increasing the aspect ratio of the shearing region. By doing so, the interval between the rotation events is considerably increased and hence one can safely measure in the strictly ordered regime, with the bubbles aligned with the shearing wheels. How this rotation is avoided in [66] we do not know, but if one looks at the experimental images in that paper, one observes that the monodisperse domains only extend over 7 — 8 bubbles due to the presence of defects, thus likely hindering large-scale collective rearrangements, while at the same time leaving enough ordered foam at the shearing boundaries to allow for rate independent shear banding.

As in the case of the bidisperse foams, we fit model profiles to our experimental data. For our model to yield rate independent velocity profiles, the drag forces need to balance in the same ratio for all driving velocities. This can only be achieved if $\beta = 2/3$ since we have already confirmed with rheometry that $\alpha = 2/3$. Indeed we find that the experimental profiles are best fit by model profiles if one fixes $k = 0.3$ and $\beta = 0.67 \pm 0.05$, see Fig. 2.13. The value of k is remarkably small. If we assume that prefactor f_{bw} for the bubble wall drag remains unchanged for the ordered foam, this means that the bubble-bubble drag prefactor f_{bb} is much larger compared to its value for a disordered foam. Note however, that the power law exponent β greatly influences the value of the drag force: for instance, if $\Delta v = 0.001$ m/s, then $(\eta v/\sigma)^{2/3} = 1.6 \times 10^{-3}$, whereas $(\eta v/\sigma)^{0.36} = 3.1 \times 10^{-2}$, which is more than an order of magnitude larger.

Disorder

We now return to the question how disorder sets the rheological behaviour in foam flows. We have shown that the average drag between bubbles scales as $v^{2/3}$ for monodisperse foams, whereas it scales as $v^{0.36}$ for bidisperse foams. On the other hand, at the bubble level, the drag forces scale as $v^{2/3}$ as is evidenced by the rheometrical data presented in 2.11(b). We speculate that this is closely connected to the non-affine behaviour of the bubbles [23,76,80]: close to the jamming transition, the shear modulus of the foam becomes anomalously large due to the fact that bubbles fluctuate much more than can be expected from the affine prediction — which is that the bubbles follow the imposed shear — and thus dissipation increases.

In our experiment, this results in an anomalous scaling of the bubble-bubble drag force, which in turn is reflected in the observed rate dependence of the velocity profiles for bidisperse foams. We can thus investigate when the rate dependence of the velocity profiles first occurs by gradually increasing the disorder in a monodisperse foam.

To this end we record velocity profiles in a monodisperse foam made of 2.7 mm size bubbles in which we gradually increase the area fraction of smaller (1.8 mm) bubbles. After mixing the two species we measure velocity profiles at $v_0 = 0.083, 0.26$ and 0.83 mm/s. We already observe the occurrence of rate dependent velocity profiles for small quantities of defects, indicating that rate independent flows are in fact limited to the singular case of completely ordered foams. We have not quantified the amount of disordered motion, but by visual inspection, we already see the swirling patterns, typical of our 50/50 bidisperse foam, occuring at 2 % disorder.

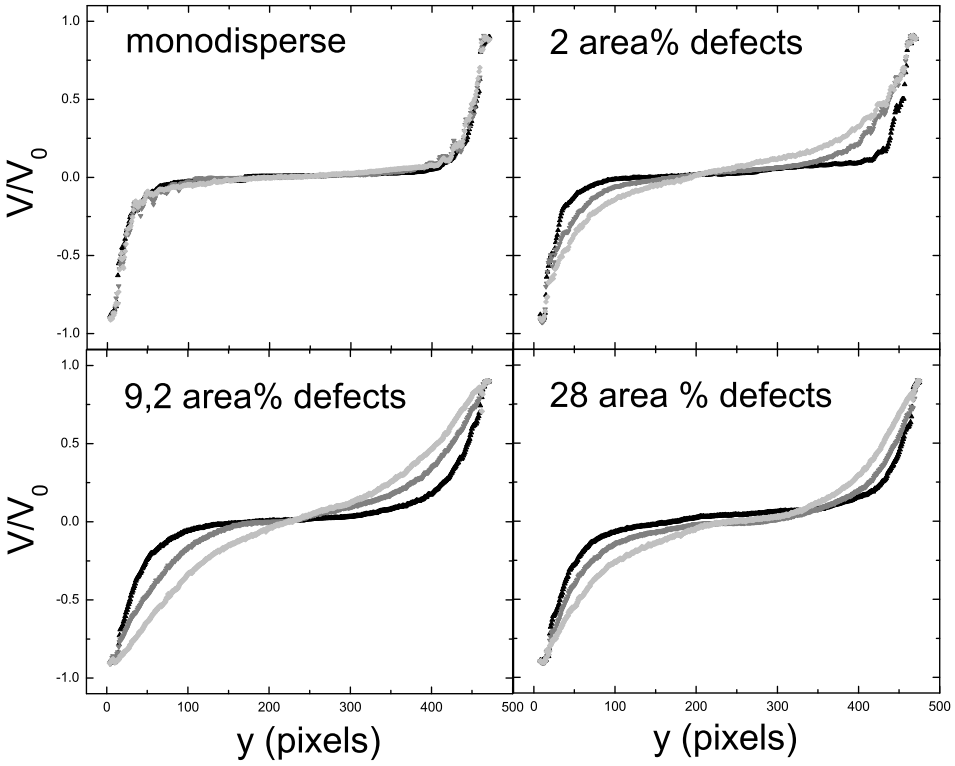

FIGURE 2.14: Velocity profiles for an ordered foam consisting of 2.7 mm bubbles for driving velocities $v_0 = 0.083$ mm/s (light gray), $v_0 = 0.083$ mm/s (dark grey) and $v_0 = 0.083$ mm/s (black) to which defects are added in the form of an increasing area fraction of 1.8 mm bubbles.